Radiat Environ Biophys (1997) 36: 105–116


ORIGINAL PAPER

**H. Tomita · M. Kai · T. Kusama · A. Ito**

# Monte Carlo simulation of physicochemical processes of liquid water radiolysis

## The effects of dissolved oxygen and OH scavenger

Received: 4 March 1996 / Accepted in revised form: 14 November 1996

**Abstract** The paper describes developments of the physicochemical part of a computer code system that estimates DNA strand break induction on plasmid pBR322 DNA. In order to test the reliability of the model, we evaluated the dielectric function and the time-dependent yield of chemical species in the presence of OH radical scavenger or dissolved oxygen. Results agree with measurements on the radiolysis of liquid water. When a hybrid model of a liquid inelastic cross-section and a vapour elastic cross-section is used, energy deposition by vibrational excitations is estimated to be approximately 11% of total energy deposition.

## Introduction

The calculation of the spatial distribution of energy depositions along the path of ionizing radiation (i.e., track structure) contributes to our deeper understanding of radiation chemistry and biology. Using Monte Carlo methods, several groups of authors have calculated the track structure in liquid water [1–3]. However, the calculated results vary among the groups appreciably [4]. This is mainly because of the uncertainties in the knowledge of electron interactions with condensed matter.

The paper presents details of a calculational model of the events that begin at about $10^{-15}$ s with the initial energy deposition by radiation in water and evolution of radical species down to $10^{-6}$ s. In order to test the reliability of the model, we evaluated the dielectric function, the collision stopping power, the range of electron tracks in liquid water, and the time-dependent yield of chemical species in the presence of OH radical scavenger or dissolved oxygen. The code TRACEL (TRACk structure of Electrons in Liquid water) covers the physical stage ($\leq 10^{-15}$ s), RADYIE (RADical YIEld) describes the physicochemical stage ($10^{-15} \sim 10^{-12}$ s), and RADIFF (RADical DIFFusion) follows the radical diffusion ($10^{-12} \sim 10^{-6}$ s).

H. Tomita (✉)* · M. Kai · T. Kusama
Department of Radiological Health, Faculty of Medicine, University of Tokyo, 7-3-1 Hongo, Bunkyo-ku, Tokyo 113, Japan

A. Ito
Department of Physics, Cancer Institute, 1-37-1 Kami-Ikebukuro, Toshima-ku, Tokyo 170, Japan

*Present address*:
* Medical Systems Research Department, Central Research Laboratory, Hitachi, Ltd., 1-280 Higashi-Koigakubo, Kokubunji-shi, Tokyo 185, Japan
e-mail: tomita@ctl.hitachi.co.jp

## Physical stage

### Inelastic collision cross-sections of liquid water

Dielectric theory was used for obtaining the cross-sections for inelastic scattering in liquid water. The response of a medium to a sudden energy transfer $\omega$ and momentum transfer $q$ is described by a complex dielectric response function $\varepsilon(q,\omega)$ [5]. While in general $\varepsilon$ may be a tensor, we assume the water medium is homogeneous and isotropic so that $\varepsilon$ is a scalar quantity which does not depend on its direction. The cross-section derived from dielectric theory is the differential inverse mean free path (DIMFP) $\tau$, viz., the probability of an energy loss $\omega$ per unit distance traveled by an electron of energy $E$ [6]. For nonrelativistic electrons,

$$\tau(E,\omega) = \frac{1}{\pi E}\int_{q^-}^{q^+} \frac{dq}{q}\,\mathrm{Im}\left(-\frac{1}{\varepsilon}\right) \tag{1}$$

where $q_\pm = \sqrt{2}\left[\sqrt{E} \pm \sqrt{E-\omega}\right]$. In the rest of this paper, we use atomic units (a.u.), where $\hbar = m = e = 1$. $\mathrm{Im}(-1/\varepsilon)$ is the energy loss function defined by

$$\mathrm{Im}\left(-\frac{1}{\varepsilon}\right) = \frac{\varepsilon_2(q,\omega)}{\varepsilon_1^2(q,\omega)+\varepsilon_2^2(q,\omega)} \tag{2}$$

where $\varepsilon_1(q,\omega)$ and $\varepsilon_2(q,\omega)$ are the real and imaginary parts of the dielectric function ($\varepsilon(q,\omega) = \varepsilon_1(q,\omega) + i\,\varepsilon_2(q,\omega)$).

Integration over the allowed values of $\omega$ yields the inelastic mean free path $\lambda$ through

$$\lambda^{-1} = \int \tau(E,\omega)\,d\omega \tag{3}$$

The stopping power is given by

$$S = \int \omega\,\tau(E,\omega)\,d\omega \tag{4}$$

The electron energy covered by TRACEL includes that of the Compton electrons of $^{60}$Co $\gamma$-ray (less than 1 MeV). No relativistic correction was considered. The dielectric response function of liquid water observed by optical measurement [7] is limited to $\varepsilon(0,\omega)$. The quadratic extension of the energy-loss function to $q > 0$ was used [6].

$$\mathrm{Im}\left(-\frac{1}{\varepsilon(q,\omega)}\right) = \int_0^\infty d\omega'\,\omega'\,\mathrm{Im}\left(-\frac{1}{\varepsilon(0,\omega')}\right)\times \frac{\delta[\omega-(\omega'+q^2/2)]}{\omega} \tag{5}$$

where $\delta$ is Dirac delta function, $\omega$ represents the energy loss, and $q$ the momentum transfer. Not the whole $(\omega - \omega')$ plane is allowed in Eq. (5). For an incident energy $E$, the allowed region of the plane is given by [8]

$$\omega \le \frac{1}{2}(E+\omega') \tag{6a}$$

$$\omega \ge \frac{1}{2}\left(E+\omega' - \sqrt{E(E-2\omega')}\right) \tag{6b}$$

$$\omega' \ge 0 \tag{6c}$$

The result of integration with the above boundary condition, together with electron-exchange correction, "exchange-corrected" DIMFP, $\tau_{\mathrm{exc}}$ is represented by [6]

$$\tau_{\mathrm{exc}}(E,\omega) = \frac{1}{2\pi E}\int_0^\infty d\omega'\,\omega'\,\mathrm{Im}\left(-\frac{1}{\varepsilon(0,\omega')}\right)\times \{F(E,\omega',\omega) + F(E,\omega',E+\omega'-\omega) - \left[F(E,\omega',\omega)\,F(E,\omega',E+\omega'-\omega)\right]^{1/2}\} \tag{7a}$$

where

$$F(E,\omega',\omega) = \theta\left(\omega - \frac{q_-^2}{2} - \omega'\right)\times \theta\left(\omega' - \omega + \frac{q_+^2}{2} - \omega'\right)/\omega(\omega-\omega') \tag{7b}$$

and $\theta(x) = 1$ for $x > 0$ and $\theta(x) = 0$ for $x < 0$. The region of $\omega - \omega'$ integration is

$$y' \ge 2y - 1 \tag{8a}$$

$$y' \le 2\sqrt{1-y}\left(1-\sqrt{1-y}\right) \tag{8b}$$

$$y' \ge 0 \tag{8c}$$

where $y = \omega/E$, $y' = \omega'/E$. The sum rules of the energy loss, or the oscillator strength,

$$\int_0^\infty d\omega\,\omega\,\mathrm{Im}\left(\frac{-1}{\varepsilon(q,\omega)}\right) = 2\pi^2 n_0 Z \tag{9}$$

where $n_0$ is the density of molecules in the medium ($4.9577 \times 10^{-3}$ a.u.), $Z$ is the number of electrons per molecule (=10). Equation (9) is satisfied if $\mathrm{Im}(-1/\varepsilon(q,\omega))$ obeys Eq. (5) [6]. Ritchie et al. [9] described the imaginary part, $\varepsilon_2(q,\omega)$, of the dielectric function, using a sum of derivative Drude functions:

$$\varepsilon_2 = \omega_p^2 \sum_n \frac{2 f_n \gamma_n^3 \omega^3}{[(E_n^2-\omega^2)^2 + \gamma_n^2\omega_n^2]^2} \tag{10}$$

where $\omega_p$ is the plasma frequency. $E_n$ are resonance energies, $\gamma_n$ are damping constants, and $f_n$ are oscillator strengths, all taken to be fitting parameters to optical data [7]. $\varepsilon_2(0,\omega)$ was partitioned into fractions corresponding to the excitations and ionization channels that are known to exist for $H_2O$ molecules. Six modes of energy absorption in liquid water, each associated with a particular excitation transition of the water molecule, together with five modes of ionization transitions are listed in Table 1. For excitation, we used the same values as Paretzke et al. [10]. For ionization, we used observed values [11] for $1b_1$, $3a_1$ and $1b_2$ ionization and estimated values [12] for $2a_1$ and $1a_1$ ionization. The parameters $\gamma_n$ and $f_n$ for ten modes, except for $1a_1$ ionization, were determined by fitting optical data [7]. The fitted curves are shown in Fig. 1, and the

**Table 1** The threshold energy of excitation and the binding energy of each transition (liquid water) assumed in this simulation

| Event | Energy (eV) | Reference |
|---|---|---|
| $\tilde{A}^1B_1$ excitation | 8.4 | Paretzke et al. [10] |
| $\tilde{B}^1A_1$ excitation | 10.1 | Paretzke et al. [10] |
| $1b_1$ ionization | 10.9 | Faubel et al. [11] |
| Rydberg (A+B) excitation | 11.26 | Paretzke et al. [10] |
| Rydberg (C+D) excitation | 11.93 | Paretzke et al. [10] |
| $3a_1$ ionization | 13.5 | Faubel et al. [11] |
| Diffuse band excitation | 14.1 | Paretzke et al. [10] |
| $1b_2$ ionization | 17.0 | Faubel et al. [11] |
| Collective excitation | 21.4 | Paretzke et al. [10] |
| $2a_1$ ionization | 26.3 | Kowari and Sato [12] |
| $1a_1$ ionization | 533 | Kowari and Sato [12] |

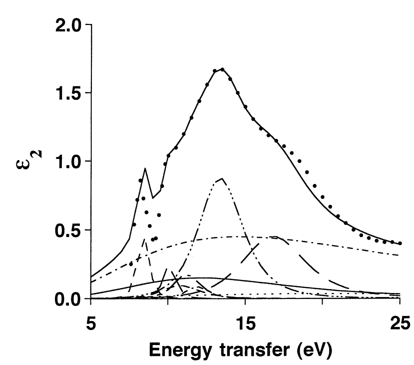


**Fig. 1** Least-square fitting of the imaginary part of the dielectric function ($\varepsilon_2$) of liquid water by a sum of the derivative Drude functions. – – - $A^1B_1$, —– - $B^1A_1$, – – - $1b_1$, — - - Ryd(A+B), ----- Ryd(C+D), – · · · · $3a_1$, —– diffuse band, — - $1b_2$, ----- collective, ·-·-· $2a_1$, —– $\varepsilon_2$ (fitted), • $\varepsilon_2$ (observed). The curve $\varepsilon_2$ (— fitted) represents the sum of all the contributions

**Table 2** Parameters for the Drude functions determined from fits to the imaginary part of dielectric function

| $n$ | Transition | $E_n$ (eV) | $\gamma_n$ (eV) | $\omega_p^2 f_n$ |
|---|---|---|---|---|
| 1 | $\bar{A}^1B_1$ excitation | 8.4 | 1.317 | 2.618 |
| 2 | $B^1A_1$ excitation | 10.1 | 1.447 | 1.825 |
| 3 | $1b_1$ ionization | 10.9 | 4.545 | 2.349 |
| 4 | Rydberg (A+B) excitation | 11.26 | 3.038 | 3.047 |
| 5 | Rydberg (C+D) excitation | 11.93 | 2.706 | 1.400 |
| 6 | $3a_1$ ionization | 13.5 | 5.298 | 31.25 |
| 7 | Diffuse band excitation | 14.1 | 21.87 | 21.44 |
| 8 | $1b_2$ ionization | 17.0 | 7.529 | 28.85 |
| 9 | Collective excitation | 21.4 | 52.91 | 210.9 |
| 10 | $2a_1$ ionization | 26.3 | 56.04 | 22.47 |
| 11 | $1a_1$ ionization | 533.0 | 659.8 | 134.8 |

parameters are listed in Table 2. Once $\varepsilon_2(0,\omega)$ was determined by the above procedure, $\varepsilon_1(0,\omega)$ was given by the Kramers-Kronig relation [9]

$$\varepsilon_1 = 1 + \omega_p^2 \sum_n f_n \frac{(E_n^2-\omega^2)[(E_n^2-\omega^2)^2 + 3\gamma_n^2\omega^2]}{[(E_n^2-\omega^2)^2+\gamma_n^2\omega^2]} \tag{11}$$

The parameters for $1a_1$ ionization were determined to be consistent with (a) the photo-ionization cross-section of $H_2O$ [13], (b) the energy-loss sum rules (Eq. 9), and (c) mean excitation energy of liquid water, 79.75 eV [14]. The photoionization cross-section [13] is for water vapour; however, the difference between vapour and liquid water can be ignored in the higher energy region. The mean excitation energy $I$ was calculated from the formula

$$\ln(I) = \frac{1}{2\pi^2 n_0 Z} \int_0^\infty \mathrm{d}\omega'\, \omega' \ln(\omega')\, \mathrm{Im}\left(\frac{-1}{\varepsilon(0,\omega')}\right) \tag{12}$$

The partial DIMFP for the $i$th mode of energy absorption, $\tau_i$, is defined by replacing $\varepsilon_2(q,\omega)$ in the numerator of the integrand of Eq. (2) by $\varepsilon_2^{(i)}(q,\omega)$ [15]. The $\varepsilon_2^{(i)}(q,\omega)$ corresponds to each ionization or excitation transition, i.e., $\varepsilon_2 = \Sigma\varepsilon_2^{(i)}$ ($n = 1, 2, \ldots, 11$). The electron-exchange correction was taken into consideration. By inserting $\tau_i$ into Eq. (3), we obtain partial IMFP, $\lambda^{-1(i)}$, for excitation and ionization (Fig. 2).

## Elastic collision cross-sections

Elastic collision cross-section was observed to be an order of magnitude smaller in amorphous ice [16]. Bolch et al. [15] suggested a scaling of vapour elastic cross-sections by 0.6 to obtain values for liquid water within the range of $E < 10$ eV. We, however, assumed elastic collision cross-sections of liquid water to be identical with the vapour phase, because we have no sufficient background for a modification.

### *Integral elastic collision cross-sections*

When the initial energy of an electron is below 1 keV, we used experimental data summarized by Märk et al. [17].

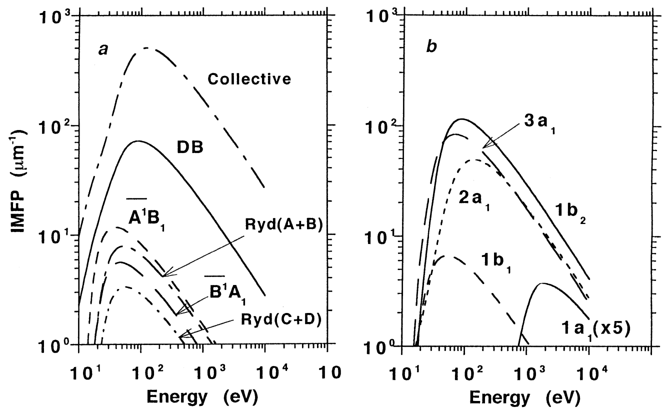


**Fig. 2** **a** Partial inverse mean free paths (IMFP) for electronic excitation used in the TRACEL program; **b** Partial IMFP for ionization used in the TRACEL program

Above 1 keV, the electron data library of the Lawrence Livermore National Laboratory [18] was used.

### *Differential elastic collision cross-sections*

The angular distribution of elastically scattered electrons was calculated using the methods of Brenner and Zaider [19] and Uehara et al. [20]. When the initial energy of an electron is below 0.2 keV, the angular distribution of elastic scattering into angle $\theta$ was described by the analytic equation

$$\left(\frac{\mathrm{d}\sigma}{\mathrm{d}\Omega}\right)_{el} \propto \frac{1}{(1+2\gamma-\cos\theta)^2} + \frac{\alpha}{(1+2\delta-\cos\theta)^2} \tag{13}$$

where $\gamma$, $\alpha$, $\delta$ are fitting parameters to experimental data [19]. Above 0.2 keV, the elastic scattering is known to be described well by the Rutherford formula, which includes a correction for atomic screening effects [19]

$$\left(\frac{\mathrm{d}\sigma}{\mathrm{d}\Omega}\right)_{el} \propto \frac{1}{(1+2\eta-\cos\theta)^2} \tag{14}$$

The screening parameter $\eta$ is given by

$$\eta = \eta_c \frac{1.7\times10^{-5} Z^{2/3} m_0 c^2}{T[T/(m_0 c^2)+2]} \tag{15}$$

where $Z$ is the atomic number, $T$ is the kinetic energy, $m_0 c^2 = 0.511$ MeV is the electron rest mass.

$$\beta^2 = 1 - \frac{1}{(T/m_0 c^2 + 1)^2} \tag{16}$$

[20] and

$$\eta_c = 1.198\,(T < 50\ \text{keV}) \tag{17a}$$

$$\eta_c = 1.13 + 3.76\,(Z/137\beta)^2\,(T \geq 50\ \text{keV}) \tag{17b}$$

In Eqs. (15), (17) the effective atomic number $Z_{\mathrm{eff}}$ was used in place of atomic number $Z$. The effective atomic number of the water molecule was assumed to be 7.42 [20].

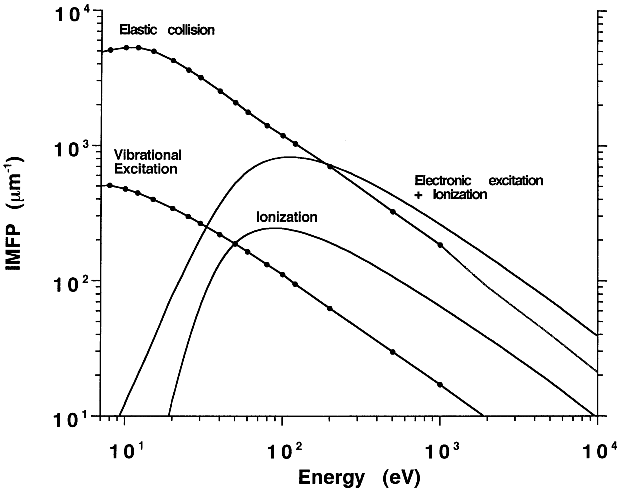


**Fig. 3** Inverse mean free paths (IMFP) or macroscopic cross sections, for elastic and inelastic scattering of electrons in liquid water. Cross sections for elastic collision (below 1 keV, taken from [17]), and above 1 keV, taken from [18]), ionization (evaluated), vibrational excitation (taken from [21]), and electronic excitation plus ionization (evaluated) are plotted

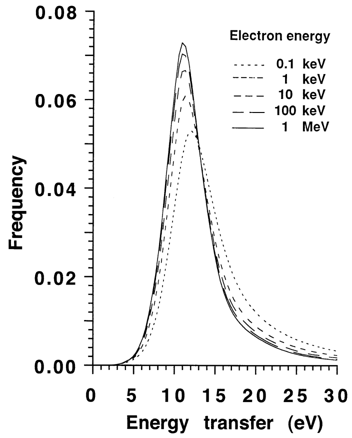


**Fig. 4** Frequency of partial differential inverse mean free paths (DIMFP) for $1b_1$ ionization (10.9 eV) as a function of electronic energy (1 MeV, 100 keV, 10 keV, 1 keV, 0.1 keV). The curves are obtained by normalization of partial DIMFPs

## Vibrational excitation cross-sections

The vibrational excitation cross-sections are of the same order of magnitude in amorphous ice as in the gas [16]. Hence, vibrational excitation cross-sections of the liquid phase were assumed to be identical with the vapour phase. It has been separated into three parts: (a) the bending mode (threshold energy 0.198 eV); (b) the stretching mode (the sum of the symmetric stretch 001 and the asymmetric stretch 001 with threshold energy 0.453 eV); (c) the lump-sum cross-section for other kinds of vibrational excitation (threshold energy 1.0 eV). We used the data compiled by Hayashi [21].

## Electron inverse mean free path

The inverse mean free paths (IMFP), or macroscopic cross-sections, for elastic, vibrational excitation, ionization, and the sum of electronic excitation and ionization in liquid water are shown in Fig. 3. Using the method mentioned above, the curves of inelastic IMFP were obtained.

## Monte Carlo procedures of TRACEL program

After the IMFP and DIMFP were determined by the procedures previously described, the spatial and temporal coordinates of an initial electron were followed. The flight distance, $s$, to a next event was determined by

$$s = -\lambda_{\text{tot}} \ln R \tag{18}$$

where $\lambda_{\text{tot}}$ is total mean free path, and $R$ is a uniform random number ($0 \le R < 1$). The type of interaction was then chosen according to the proportion of the IMFP shown in Fig. 3.

If the event is an elastic collision, the electron energy remains unaltered, and the polar angle $\theta$ of the direction into which the electron scattered was determined from Eqs. (13)–(17). The azimuthal angle $\phi$ was assumed to be uniformly distributed between 0 and $2\pi$.

In a vibrational excitation event, the electron energy was reduced by the threshold energy (0.198, 0.453, 1.0 eV). In an electronic excitation event, the electron energy was reduced by the energy transfer $\omega$ determined by random sampling from the probability density function of the partial DIMFP of the event at that electron energy. Figure 4 shows the probability density function of the $1b_1$ ionization (10.9 eV). The peak width of the curves decreased with the increase of electron energy. The direction of an electron was assumed to be unchanged both in vibrational and electronic excitation events. If the energy loss is less than 50 eV, a delocalization of the energy transfer was assumed to occur [1]. This delocalization is a consequence of collective effects and was modeled by displacing the interaction site through a lateral distance $b$ in a random azimuthal to the incident electron's path. The distance $b$ was chosen from the distribution [1]

$$P(b)\,\mathrm{d}b = C\,\frac{\exp(-\omega b / v\gamma)}{b_0^2 + b^2}\,b\,\mathrm{d}b \tag{19}$$

where $\omega$ is the energy loss, $v$ is the electron speed, and $b$ and $\gamma$ are constants (taken to be 0.2 nm and 5, respectively). $C$ is a normalization constant chosen such that

$$\int_0^{b_{\max}} P(b)\,\mathrm{d}b = 1 \tag{20}$$

$b_{\max}$ was chosen to be 10 nm [1]. A collective excitation event (21.4 eV) creates a secondary electron whose kinetic energy is large enough to additionally ionize the water medium. Except for collective excitation, the energy transfer is relatively small so that a subexcitation electron $e^-_{sub}$ (< 7.4 eV) is created most often. Thus, the motion of the secondary electron created by the collective excitation event, through the autoionization process, was also followed in the code.

In an ionization event, the electron's energy was reduced by the energy transfer selected. The secondary electron's kinetic energy was given the energy transfer by the primary electron minus the binding energy of the target electron (Table 1). The directions of the primary and secondary electrons with respect to the primary particle were determined using the methods of Grosswendt and Waibel [22]. The azimuthal angle $\phi_p$ of the primary electron was uniformly distributed between 0 and $2\pi$, and the azimuthal angle $\phi_s$ of the secondary was $\phi_p - \pi$. The polar angles $\theta_p$ and $\theta_s$ of the two particles were evaluated using the following expressions:

$$\sin^2\theta_p = \frac{k/T}{(1-k/T)\,T/(2m_0c^2)+1} \tag{21}$$

$$\sin^2\theta_s = \frac{1-k/T}{1+k/(2m_0c^2)} \tag{22}$$

where $T$ is the kinetic energy of primary electron after collision and $k$ is the kinetic energy of secondary electron. This process is continued until all of the original electron's energy is spent and falls below 7.4 eV, which is assumed to be a threshold for electronic excitation in liquid water [23].

## Physicochemical stage

In the physicochemical (prechemical) stage, during the period between $10^{-14}$ and $10^{-12}$ s, the species $H_2O^+$, $H_2O^*$, and $e^-_{sub}$ are converted into other chemical species by the RADYIE program. This program considers the thermalization and hydration of $e^-_{sub}$, dissociation and autoionization process of $H_2O^*$.

### Decay channels of water molecule

A molecule that has received energy exceeding its ionization threshold ($I_p$) does not necessarily ionize because there are other decay channels such as dissociation into neutral fragments, and the ionization process competes with the neutral fragmentation [24]. The quantum yield $\eta$ for ionization of water molecules increases with the increase of energy and probably reaches 1.0 at around 11.64 to 17.06 eV in the liquid phase [25]. The quantum yield $\psi$ means the ratio of photoionization cross-section $\sigma_i$ to photoabsorption cross-section $\sigma_a(\psi=\sigma_i/\sigma_a)$. Hence, Rydberg state, diffuse band, and collective excitation events have a high efficiency of producing $H_2O^+$ through the autoionization process. Collective excitation (21.4 eV) was assumed to be a plasmon-type excitation (e.g., [3]) in several earlier studies. The plasmons may decay into single or plural ionization or excitations [26], but there is no evidence for plasmon excitation in liquid water [27]. However, to match the experimentally determined initial yields of chemical products, the scheme shown in Table 3 for partitioning of $H_2O^*$ into dissociations and autoionizations was adopted. We assumed that 30% of collective excitation produces both $H_2O^+$ and dissociated molecules (H + OH).

**Table 3** Assumed partitioning of excitations in RADYIE. Each collective excitation was assumed to produce a secondary electron (through $1b_1$ event)

| | | |
|---|---|---|
| $\tilde{A}^1B_1$ | $H_2O^* \rightarrow H + OH$ | 75% |
| | $H_2 + O$ | 25% |
| $\tilde{B}^1A_1$ | $H_2O^* \rightarrow H_2 + O$ | 100% |
| Rydberg, DB | $H_2O^* \rightarrow H_2O^+$ + e(sub)- | 100% |
| Collective | $H_2O^* \rightarrow H + OH$ | 30% |
| | $H_2O + \Delta E$ | 70% |

### Procedures in RADYIE program

All ionizations (direct ionization and autoionization) were assumed to produce $H_2O^+$ ions.

$$H_2O^+ + H_2O \rightarrow H_3O^+ + OH \tag{23}$$

When a $H_2O^+$ is formed, it is first allowed to migrate in a random direction through a distance selected from a Gaussian distribution with a mean displacement 1.25 nm [15], which corresponds to the radial distribution function [23]

$$f(R) = \frac{\sqrt{2}}{\sqrt{\pi d^3}}\, R^2 \exp\left(\frac{-R^2}{2d^3}\right) \tag{24}$$

where the mean radial distance $\langle R\rangle$ is given by $2d\sqrt{(2/\pi)}$.

The $H_3O^+$ was assumed to be at the same position as the $H_2O^+$, and the OH radical was positioned with random orientation at a distance of 0.29 nm [28], which corresponds to the diameter of a water molecule. $H^+_{aq}$ was assumed to be at the same position as the $H_3O^+$ [29].

In the dissociation of an excited water molecule into H and OH radicals, the products were assumed to be separated by 0.87 nm on a randomly oriented line centered at the original site of $H_2O^*$, and as well as in the case of $H_2$ and O by 0.58 nm [28, 30].

### Thermalization of subexcitation electrons

The RMS (root mean square) thermalization distance $l_{th}$ (E) was assumed to obey the theoretical curve described by Ritchie et al. [31]. The comparison between the theoretical curve and other observed data is also shown in Ritchie et al. [31]. A hydrated electron was moved in a random direction at a distance $R_{th}$ from the $H_2O^+$ position. The distance $R_{th}$ was selected from the distribution of Eq. (24) so that $l_{th}$ is equal to $3b^2$.

## Chemical stage

Independent reaction times (IRT) method

The RADYIE program was applied to calculate the spatial coordinates of the radicals H, OH, $H^+_{aq}$, $e^-_{aq}$, and O. The RADIFF programs read these coordinates as input data and treat the diffusion and reactions during the period between $10^{-12}$ and $10^{-6}$ s in a manner described by the Smoluchowski relation, i.e., assuming the two radicals interact whenever the distance becomes less than a reaction radius $a$. The reaction radius was estimated by $k = 4\pi a D'$ for different species and $k = 2\pi a D'$ for identical species, where $k$ is the reaction rate and $D'$ is the relative diffusion coefficient. If the diffusion and the potential energy of interaction of the pair are spherically symmetrical, the reaction probability $W(x, a, t)$ is a function only of the initial separation of the pair $x$, the time $t$, and the reaction radius $a$. The probability $W(x, a, t)$ is given by [32]

$$W(x,a,t) = \frac{a_{\text{eff}}}{x_{\text{eff}}}\, erfc\left(\frac{x_{\text{eff}} - a_{\text{eff}}}{\sqrt{4D't}}\right) \tag{25}$$

where $x_{\text{eff}} = x$ and $a_{\text{eff}} = a$ for a diffusion-controlled reaction which is not affected by a coulombic interaction. The diffusion-controlled reactions between repulsive ions were modeled using Eq. (25), by evaluating $x_{\text{eff}}$ and $a_{\text{eff}}$ from the equation [33]

$$a'_{\text{eff}} = \frac{-r_c}{1 - \exp(r_c / a_{\text{eff}})} \tag{26}$$

$$x'_{\text{eff}} = \frac{-r_c}{1 - \exp(r_c / x_{\text{eff}})} \tag{27}$$

The quantity $r_c$ is the Onsager distance defined by

$$r_c = \frac{Z_1 Z_2 e^2}{4\pi \varepsilon_0 \varepsilon_r k_B T} \tag{28}$$

where $Z_1 e$ and $Z_2 e$ are the ionic charges, $\varepsilon_0$ is the permittivity of free space, $\varepsilon_r$ is the relative permittivity of the medium, $k_B$ is the Boltzmann constant, and $T$ the temperature. The reactions between attractive ions such as

$$e^-_{aq} + H^+_{aq} \rightarrow H \tag{29}$$

$$H^+_{aq} + O_2^- \rightarrow HO_2 \tag{30}$$

$$H^+_{aq} + O^- \rightarrow OH \tag{31}$$

$$H^+_{aq} + O_2^- \rightarrow H_2O_2 \tag{32}$$

are thought to be partially diffusion-controlled reactions. This means that the pair does not react instantaneously on an encounter, so that a partially reflecting boundary condition is needed. A value of 0.5 nm was chosen for $a$, then the reaction velocity $v$ was estimated by [33]

$$k = \frac{4\pi D' a^2 v}{a v + D'} \tag{33}$$

The partially diffusion-controlled reactions were modeled using Eq. (25), by evaluating $x_{\text{eff}}$ and $a_{\text{eff}}$ from the equation [33]

$$a''_{\text{eff}} = \frac{-r_c}{1 - \exp(r_c / a)\,(1 + D' r_c / v a^2)} \tag{34}$$

$$x''_{\text{eff}} = \frac{-r_c}{1 - \exp(r_c / x_{\text{eff}})} \tag{35}$$

Except for (29), the reactions (30)–(32) were relatively unimportant because of the small yields of $O_2^-$, $O^-$, and $HO_2^-$, and the effect was small. The random reaction time $T_r$ was determined by solving Eq. (25) as

$$\begin{aligned} T_r &= \frac{1}{4D}\left[\frac{x_{\text{eff}} - a_{\text{eff}}}{erfc^{-1}(\xi x_{\text{eff}} / a_{\text{eff}})}\right]^2 (\xi < a_{\text{eff}} / x_{\text{eff}}) \\ &= \infty\ (\xi \geq a_{\text{eff}} / x_{\text{eff}}) \\ &= 0\ (x_{\text{eff}} \leq a_{\text{eff}}) \end{aligned} \tag{36}$$

where $\xi$ is a random number uniformly distributed between 0 and 1 and $\text{erfc}^{-1}(x') = x$ is the inverse of $\text{erfc}(x) = x'$ [33]. The probability of the reaction is largest when $T_r$ is the smallest. The table of $T_r$ was sorted into ascending order, and the first reaction was decided to occur, then removed from the table (the radicals are diminished after reaction). When new radicals were created (e.g., $H + O \rightarrow OH$), they were added to the table. This table was scanned until a possible reaction was found, then the above procedures were repeated. Thirteen chemical species (H, OH, $H^+_{aq}$, $e^-_{aq}$, $OH^-$, $H_2O_2$, O, $O_2$, $O_2^-$, $HO_2$, $HO_2^-$, $O^-$, Tris) were considered in the RADIFF program. The diffusion coefficients were taken from Elliot et al. [34] and Hill and Smith [29]. Thirty-four chemical reactions were considered in the program (33 reactions were the same as Hill and Smith [29] and the reaction between OH and Tris was also considered). The reaction rate constants were from Buxton et al. [35].

Locations of species after reaction

When a reaction occurs between a pair of species located at positions $(x_1, y_1, z_1)$ and $(x_2, y_2, z_2)$, the reaction site was placed midway along the line segment connecting their positions. The coordinates of the reactants were weighted inversely by their diffusion coefficients. The $x$ coordinate of the reaction site $x_r$ was given by [15]

$$x_r = x_1\left(\frac{\sqrt{D_2}}{\sqrt{D_1} + \sqrt{D_2}}\right) + x_2\left(\frac{\sqrt{D_1}}{\sqrt{D_1} + \sqrt{D_2}}\right) \tag{37}$$

The same weighting factors were used to determine the y- and z-coordinates of the reaction site. When a single radical is created in the reaction (e.g., $H + O_2 \rightarrow HO_2$), the coordinate of a new product was assumed to be the same as the reaction site defined by Eq. (37). When two radicals are created in the reaction, the coordinates of products were determined using reflecting boundary conditions [36].

### Tris and Oxygen reaction

In IRT simulation, for the realization of a system of $n_p$ particles, it is necessary to consider $n_p(n_p-1)/2$ reaction times by Eq. (36). When modeling scavenger reactions, it is also necessary to include $n_s$ OH scavenger particles, and consider the reaction

$$\mathrm{OH} + \text{scavenger} \rightarrow \text{removal of OH} \quad (38)$$

The total number of the combination was too large to handle even at dilute scavenger concentrations, so we treated the scavenger as a continuum, then each radical was initially surrounded by a homogeneous distribution of scavengers. The time-dependent probability that it will be scavenged before time $t$, $W_{\mathrm{scav}}$, was described by [37]

$$W_{\mathrm{scav}}(t) = 1 - \exp\left(-4\pi D' a_{\mathrm{eff}}\, c_s \left[t + 2a_{\mathrm{eff}}\sqrt{\frac{t}{\pi D'}}\right]\right) \quad (39)$$

where $c_s$ is the scavenger concentration (mol dm$^{-3}$). Oxygen is a scavenger of H radicals and hydrated electrons in the reactions

$$\mathrm{H} + \mathrm{O_2} \rightarrow \mathrm{HO_2} \quad (40)$$

$$\mathrm{e^-_{aq}} + \mathrm{O_2} \rightarrow \mathrm{O_2^-} \quad (41)$$

Equation (39) was also used in the oxygen-scavenger reactions. When $O_2$ is present, each H and $e^-_{aq}$ was given a chance to be scavenged. When scavenging occurs, the species are replaced by $HO_2$ or $O_2^-$. The pressure of oxygen gas above the water was assumed to be in equilibrium with dissolved oxygen. The concentration of dissolved oxygen at atmospheric pressure was taken from a chemistry handbook [38]. At a different pressure, the concentration of dissolved oxygen was determined according to Henry's law.

### Calculations for $^{60}$Co $\gamma$-ray irradiation

For example, we calculated the $^{60}$Co $\gamma$-ray irradiation to the solutions in polypropylene tubes. By taking into consideration the attenuation coefficient of the $\gamma$-ray in both polypropylene and water, negligible spectral attenuation is assumed to occur throughout the irradiated samples. The initial electron spectrum for $^{60}$Co $\gamma$-ray was thus calculated by the photon Monte Carlo program (Hokenkan) using a bienergetic input spectrum of 1.17- and 1.33-MeV photons. The distribution of this spectrum was normalized, and the initial energy of electrons for the TRACEL program were selected randomly from this distribution. Ten track structures with starting energies sampled by the above-mentioned method were generated from random points in a large cube (5×5×5 mm) to random directions. The large cube is subject to a periodic boundary condition. The coordinates of vibrational excitations, electronic excitations, ionizations, and subexcitation electrons were included in this track structure. After that, one cube which has the same size as a simulation cell (1×1×1 μm) was generated repeatedly at random positions in the large cube, until the total energy deposition gathered in the cube came to a prescribed value (e.g., 100 Gy).

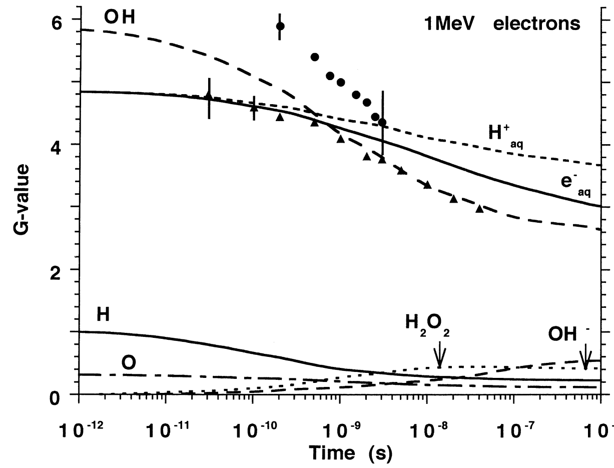


**Fig. 5** Comparison of calculated and measured time-dependent yields of H, OH, $e^-_{aq}$, $OH^+_{aq}$, $OH^-$, $H_2O_2$, and O for 1 MeV electrons in liquid water. Reactions (40) and (41) are ignored. Measured values (OH ● and $e^-_{aq}$ ▲) are taken from [39–41]

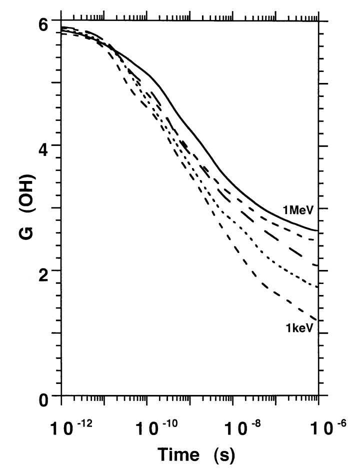


**Fig. 6** Time-dependent yields of the OH radical for electrons of initial energy $E_0$ (1 MeV, 100 keV, 25 keV, 10 keV, and 1 keV) in liquid water. Reactions (40) and (41) are ignored

## Results

### G-values

The time variations of the calculated G-values for an entire track generated by 1-MeV electrons are shown in Fig. 5 (reactions (40), (41) are ignored). The calculated initial ($10^{-12}$ s) and primary ($10^{-7}$ s) yields for 1-MeV electron in liquid water were 5.89 and 2.76 for G(OH), 4.88 and 3.18 for G($e^-_{aq}$), 0.96 and 0.24 for G(H). Time-dependent yields of OH for electrons of several energies in liquid water are shown in Fig. 6 (reactions (40), (41) are ignored). The primary yield of chemical species decreased with the decrease of the initial energy of the electron.

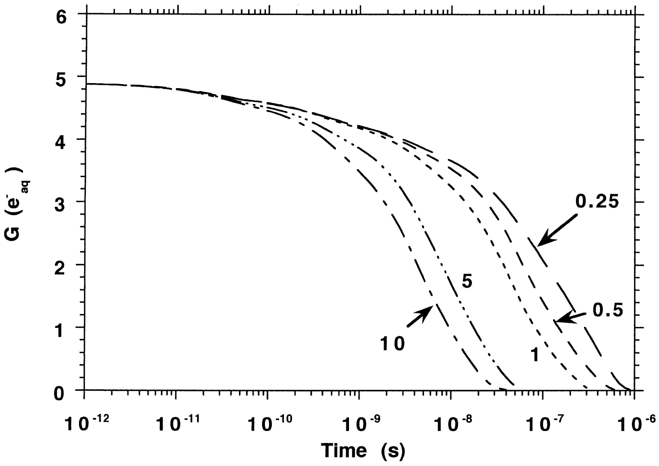


**Fig. 7** Calculated time-dependent yields of $e^-_{aq}$ as functions of atmospheric pressure at the surface of water, at 100 Gy $^{60}$Co $\gamma$-rays. Atmospheric pressures at the surface of water are 10, 5, 1, 0.5, and 0.25 atm

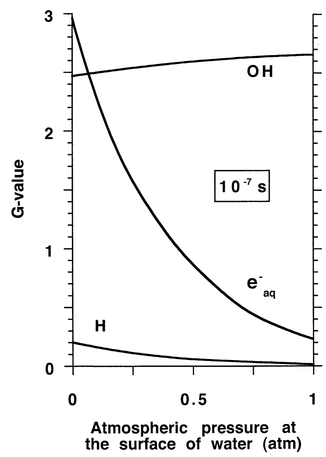


**Fig. 8** Yields of OH, H and $e^-_{aq}$ at $10^{-7}$ s as functions of atmospheric pressure at the surface of water, at 100 Gy of $^{60}$Co $\gamma$-rays

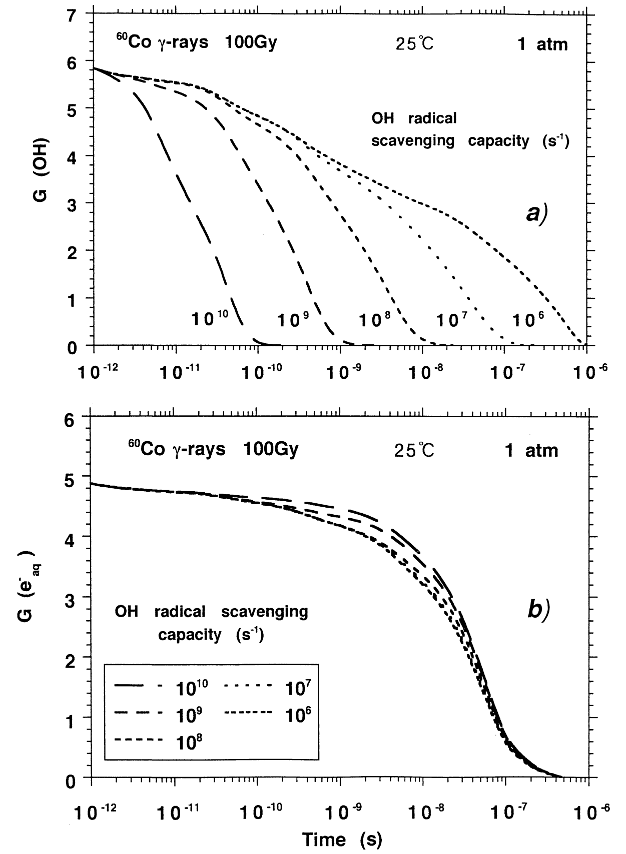


**Fig. 9** **a** Effect of the OH radical scavenger on the time-dependent yield of OH at 1 atm in air, at 100 Gy of $^{60}$Co $\gamma$-rays. The scavening capacities of OH radical scavenger are $10^{10}$, $10^9$, $10^8$, $10^7$, and $10^6$ $s^{-1}$; **b** Effect of the OH radical scavenger on the time-dependent yield of $e^-_{aq}$ at 1 atm in air, at 100 Gy of $^{60}$Co $\gamma$-rays

Dissolved oxygen

Yields of $e^-_{aq}$ as a function of time for 100-Gy $^{60}$Co $\gamma$-ray exposure at several values of atmospheric pressure at the surface of water are shown in Fig. 7. Figure 8 gives yields at $10^{-7}$ s for OH, $e^-_{aq}$, and H as a function of atmospheric pressure at the surface of water. Although G(OH) at $10^{-7}$ s was almost constant, G($e^-_{aq}$) and G(H) were strongly influenced by the atmospheric pressure at the surface of water.

OH scavenger concentration

Figure 9 shows the time-dependent yields of OH and $e^-_{aq}$ at several values of OH scavenger concentration at 1 atm. The concentration of OH scavenger is expressed by scavenging capacity ($s^{-1}$). Although OH scavengers do not interact with $e^-_{aq}$, G($e^-_{aq}$) was influenced by the concentration of the OH scavenger. This is a result of the decrease in the frequency of interactions between OH and $e^-_{aq}$.

## Discussion

The main aim of our research was to develop a calculational model of the events that begin at about $10^{-15}$ s with the initial energy deposition by radiation in water and end at $10^{-6}$ s with the completion of the radical reaction that causes DNA damage. This is the physicochemical part of a computer code system that estimates DNA strand break induction on plasmid pBR322 DNA. In order to verify the reliability of this model, we evaluated the dielectric function and the time-dependent yield of chemical species in the presence of OH radical scavenger, or dissolved oxygen. Other important findings are (1) delocalization of initially unlocalized excitations changes slightly the yield of OH radical at $10^{-6}$ s, (2) the energy deposition by vibrational excitation is approximately 11% of the total energy-deposition events. The discussion will focus on these findings. Some of the fundamental knowledge needed to obtain a more reliable track-structure in liquid water is also discussed.

## Track-structure calculation

We have studied the history of track-structure simulation and are impressed by the Oak Ridge group's study for liquid water track structure (OREC code) because of its novelty and potential power. It was, however, difficult to reproduce their study without added information. The theory of our new code is basically the same as the OREC code, but the cross-sectional data were newly evaluated. We evaluated the cross-sectional data from the combination of four items listed as follows:

1. The quadratic extension of the energy-loss function to $q > 0$ (Eq. 5) [6];
2. The imaginary part of the dielectric function is described by using a sum of the derivative Drude Function (Eq. 10) [1];
3. The fitting parameters of the derivative Drude function for ionization are taken from observed values [11] for $1b_1$, $3a_1$, and $1b_2$ ionization and estimated values [12] for $2a_1$ and $1a_1$ ionization;
4. The mean excitation energy of liquid water is 79.75 eV [14].

Ritchie et al. [1] did not clearly describe what kind of extension of the energy-loss function to $q > 0$ they used. The most plausible liquid-water cross-section was given by the fitting of the dielectric function using parameters of items 3 and 4. This was verified in view of the collision stopping power (data not shown), the range of electron track (data not shown), and the time-dependent yield of chemical species.

A number of techniques are available for the simulation of the trajectories of diffusion particles. We believe the IRT method [33] is the most computer-efficient algorithm. The comparison between IRT simulation and full-random-flight Monte Carlo simulation was performed by Clifford et al. [42], and they guaranteed the equivalence of both methods. The calculated initial, primary yields and the time-dependent yields of chemical species were found to be consistent with the knowledge of liquid water radiolysis [39–41]. The primary yield of chemical species decreased with the decrease of the initial energy of the electron (Fig. 6). Watanabe et al. [43] measured the oxidation yield of ferrous ion in a Fricke solution in the soft x-ray region from 1.8 to 10 keV. The yield of the ferrous ion decreased with the decrease of x-ray energy. The yield of $G(Fe^{3+})$ can be expressed as a linear combination of the yields of water radicals by

$$G(Fe^{3+}) = G(OH) + 3G(e^-_{aq}) + 3G(H) + 2G(H_2O_2) \quad (42)$$

The calculated yield of the ferrous ion showed the same tendency with this experiment (data not shown).

Several groups have developed methods of calculating the thermalization length of subexcitation electrons [15, 31, 44, 45]. We chose Ritchie's method [31] and used the distribution function of Goulet and Jay-Gerin [23], because their theoretical curve showed good agreement with experiments.

Turner et al. [30] also calculated the effect of dissolved oxygen and showed similar results. In their calculation, the rate constants were treated as a constant with respect to time. However, the time dependence of the rate constant for the reaction $e^-_{aq} + O_2$ was described as important in modeling scavenging reactions [46]. Hence, we used the time-dependent rate constant $k(t)$. In our calculation, not much difference was found with the result based on a time-dependent rate constant. Turner et al. [30] used the pressure of 0.209 atm as the partial pressure of $O_2$ in atmospheric air and assumed it to be in equilibrium in solvent. By contrast, the solubility of $N_2$ and $O_2$ at 25 °C in atmosphere is 1.10 and 0.57, respectively [38]. The solubility of $O_2$ is a more relevant index than partial pressure, and therefore our calculation is more realistic.

We used the IRT method and treated the scavenger as a continuum [37]. The time-dependent yield of G(OH), shown in Fig. 9, agrees with deterministic calculations [47]. This continuum approximation appears to be appropriate even in dilute aqueous solution: the OH scavenging capacity is $\sim 10^6\ s^{-1}$. A measured lifetime for the OH radical in mammalian cells is 8.7 ns [48]. The concentration of OH-radical scavenger in cells is estimated to be $\sim 10^9\ s^{-1}$ by a plasmid DNA experiment [49]. The inverse of the scavenging capacity of $10^9\ s^{-1}$ is 1 ns. Hence, DNA break induction in the cellular environment can be estimated by the decay curve of the OH radical, which corresponds to $10^9\ s^{-1}$ scavenging capacity in the first step.

The assumption that the direction remains unchanged upon vibrational and electronic excitation may be inappropriate especially in the low-energy region. The calculated results (range, stopping power, G(OH) and $G(e^-_{aq})$ at $10^{-7}$ s), however, were not much altered when an isotropic change in the direction at an excitation event was assumed for electrons below 50 eV.

## Delocalization of initially unlocalized excitations

The wavelength of slow electrons, less than 50 eV, is longer than the van der Waals size of a water molecule. For this reason, swift electrons may create excitations initially unlocalized at the trajectory of the track. Such excitations might migrate appreciable distances before localizing [1]. Although the localization of initially unlocalized excitations in water is far from being well understood, the algorithm of implementation of this phenomenon for Monte Carlo simulation has been developed [1]. The authors stated that this algorithm can be useful until additional data become available. Hence, we also used Eq. (19) and evaluated the effect of the delocalization in time-dependent yield of chemical species. Consequently, the decays of $e^-_{aq}$ and OH radical were slightly slower when delocalization was considered (data not shown). At $10^{-6}$ s, G(OH) was increased about 0.1. This is because the algorithm of delocalization scatters the initial positions of radicals. In IRT simulation, reaction probabilities are evaluated only by the distances between species. The more sparse the spatial distribution is, the slower the decay rate of the chemical species. The distribution $P(b)$ of the delocalization distance has a peak centered at 0.2 nm, and $b$ is mostly smaller than 1 nm (see Fig. 2 of [50]). The $b$ value was so small that not much difference was shown when delocalization was considered.

## Energy deposition by vibrational excitations

Vibrational excitation cross-sections of liquid water were assumed to be identical with the vapour phase. This assumption is justified by the measurement of amorphous ice films at 14 K being of the same order of magnitude as in the gas phase [16]. Hence, we used the cross-sections shown in Fig. 3 for the first-order approximation. The threshold energies of vibrational excitation are smaller than 1 eV. The frequencies of vibrational-excitation events, however, were an order of magnitude larger than the frequencies of electronic excitations and ionizations in our calculation. Consequently, the energy depositions by vibrational excitation rose up to approximately 11% of total energy-deposition events. We assumed elastic collision cross-sections of liquid water to be identical with the vapour phase. The frequency of elastic collision is approximately 90% (Fig. 3) in the region of $E < 10$ eV. The ratio of vibrational excitation cross-section to elastic collision cross-section is decisive for a result of 11%. This value will be altered after additional data are provided.

## Critique of track-structure model in liquid water

Since not all of the needed information exists, the model contains many uncertainties. Three aspects are discussed here.

### *Fitting by the derivative Drude function*

The fitting procedure by the derivative Drude function has three major problems. These are: (1) the validity of applying the derivative Drude function has not been thoroughly examined; (2) the appropriate set of $E_n$ (fitting parameter; resonance energy) of the derivative Drude function is unknown; and (3) some of the $\gamma_n$ values are comparable to, or even greater than, the corresponding $E_n$ values when the ordinary Drude function was used (data not shown) and the derivative Drude function was used (Table 2). This does not make sense for an ordinary Drude function. The derivative Drude function may have been introduced by the Oak Ridge group to avoid such contradictions. Ritchie et al. [9] pointed out that the analytical form used in Eq. (10) is more appropriate than the straightforward Drude function; however, there is no theoretical background for Eq. (10). Both Eqs. (10) and (11) are originally equivalent in the Kramers-Kronig relation. The results found by fitting the imaginary part of the dielectric function (Eq. 10) varied, however, from the results obtained by fitting the real part of the dielectric function (Eq. 11). The fitting was not convergent when both the real and imaginary parts of the dielectric function were used simultaneously. The fitting method contains essential problems.

When a series of $E_n$ of the derivative Drude function was fixed, the other parameters ($\gamma_n$ and $\omega_p^2 f_n$) were determined by least-squares fitting without much deviation. Hence, the reliability of fitted results depends on the validity of the selection of $E_n$ values. Our fitting of the dielectric function is similar to previous studies [51, 52], and the partial IMFP is also similar to Kutcher and Green [51]. It is interesting that similar results were obtained even though different fitting-functions were used in the previous studies. Note that the results of fitting were easily altered by a slight alteration of $E_n$. The limitation of each peak width of the derivative Drude function may be needed, but we believe neither theoretical nor experimental knowledge has been presented until now.

### *Collective excitation*

We assumed that 30% of the collective excitation produces both $H_2O^+$ and dissociated molecules ($H + OH$) to match the experimentally suggested initial yield of chemical reactant (Table 3). With this definition, our model involves plasmon excitation. There is considerable evidence against plasmon excitation in liquid water [27]. However, nothing is known about the mechanism of this process.

### *Elastic and vibrational excitation cross-section*

As discussed above, the ratio of vibrational excitation cross-section to elastic collision cross-section influences the total amount of energy transfer by vibrational excitation. Moreover, the elastic (nuclear) collision is the principal physical process that causes electron paths to be tortuous [53]. This means that the track lengths of electrons are readily altered by total and angular distribution of elastic collision cross-sections. We must emphasize that the TRACEL program is a hybrid model of a liquid inelastic, a vapour vibrational excitation, and a vapour elastic collision cross-section.

**Acknowledgements** Allocation of computer time at the Cancer Institute, Japanese Foundation for Cancer Research, is gratefully acknowledged. We thank Prof. Dr. Y. Hatano for helpful discussions and encouragement. We thank Dr. M. Inokuti for suggestive comments.

## References

1. Ritchie RH, Hamm RN, Turner JE, Wright HA, Bolch WE (1991) Radiation interactions and energy transport in the condensed phase. In: Glass WA, Varma MN (eds) Physical and chemical

mechanisms in molecular radiation biology. Plenum Press, New York, pp 99–133
2. Terrissol M, Beaudre A (1990) Simulation of space and time evolution of radiolytic species induced by electrons in liquid water. Radiat Prot Dosim 31: 171–175
3. Kaplan IG, Sukhonosov VYa (1991) Simulation of the passage of fast electrons and the early stage of water radiolysis by the Monte Carlo method. Radiat Res 127: 1–10
4. Nikjoo H, Terissol M, Hamm RN, Michalik V, Paretzke HG, Turner JE, Bigldeev EA, Goodhead DT (1994) Comparison of energy deposition in small cylindrical volumes by electrons generated by Monte Carlo track structure codes for gaseous and liquid water. Radiat Prot Dosim 52: 165–169
5. Bassani F, Altarelli M (1983) Interaction of radiation with condensed matter. In: Koch EE (ed) Handbook on synchrotron radiation, Vol 1, Chapter 7. North-Holland, Amsterdam
6. Ashley JC (1990) Energy loss rate and inelastic mean free path of low-energy electrons and positrons in condensed matter. J Electron Spectrosc Rel Phenom 50: 323–334
7. Heller JM, Hamm RN, Birkhoff RD, Painter LR (1974) Collective oscillation in liquid water. J Chem Phys 60: 3483–3486
8. Green NJB, LaVerne JA, Mozumder A (1988) Differential track structure of electrons in liquid water. Radiat Phys Chem 32: 99–103
9. Ritchie RH, Hamm RN, Turner JE, Wright HA (1978) The interaction of swift electrons with liquid water. In: Booz J, Ebert HG (eds) Sixth symposium on microdosimetry. Commission of the European Communities, Harwood, London, pp 345–354
10. Paretzke HG, Goodhead DT, Kaplan IG, Terrissol M (1995) Track structure quantities. In: Atomic and molecular data for radiotherapy and radiation research, Chapter 9. (IAEA-TECDOC-799) IAEA, Vienna
11. Faubel M, Steiner B (1994) Photoelectron spectroscopy at liquid water surfaces. In: Christophorou LG, Illenberger E, Schmidt WF (eds) Linking the gaseous and condensed phases of matter. The behavior of slow electrons. (NATO ASI Series B-326) Plenum Press, New York, pp 517–523
12. Kowari K, Sato S (1978) The spatial distribution of secondary electrons produced in the $\gamma$-radiolysis of water. Bull Chem Soc Jpn 51: 741–747
13. Terrissol M, Bordage MC, Caudrelier V, Segur P (1989) Cross-sections for 0.025eV–1keV electrons and 10eV–1keV photons. In: Atomic and molecular data for radiotherapy. (IAEA-TEC-DOC-506) IAEA, Vienna, pp 218–232
14. Paul H, Berger MJ (1995) Stopping powers, ranges and straggling. In: Atomic and molecular data for radiotherapy and radiation research, Chapter 7. (IAEA-TECDOC-799) IAEA, Vienna
15. Bolch WE, Turner JE, Yoshida H, Bruce Jacobson K, Hamm RN, Wright HA, Ritchie RH, Klots CE (1988) Monte Carlo simulation of indirect damage to biomolecules irradiated in aqueous solution – the radiolysis of glycylglycine. (ORNL/TM-10851) Oak Ridge National Laboratory, Oak Ridge
16. Michaud M, Sanche L (1987) Absolute vibrational excitation cross sections for slow-electron (1–18 eV) scattering in solid $H_2O$. Phys Rev A 36: 4684–4699
17. Märk TD, Hatano Y, Linder F (1995) Electron collision cross sections. In: Atomic and molecular data for radiotherapy and radiation research, Chapter 3. (IAEA-TECDOC-799) IAEA, Vienna
18. Perkins ST, Cullen DE, Seltzer SM (1991) Tables and graphs of electron-interaction cross sections from 10 eV to 100 GeV derived from the LLNL evaluated electron data library (EEDL), Z = 1 – 100. (UCRL-50400 Vol 31) Lawrence Livermore National Laboratory
19. Brenner DJ, Zaider M (1983) A computationally convenient parameterization of experimental angular distributions of low energy electrons elastically scattered off water vapour. Phys Med Biol 29: 443–447
20. Uehara S, Nikjoo H, Goodhead DT (1993) Cross-sections for water vapour for the Monte Carlo electron track structure from 10 eV to the MeV region. Phys Med Biol 38: 1841–1858
21. Hayashi M (1989) Electron collision cross-sections for atoms and molecules determined from beam and swarm data. In: Atomic and molecular data for radiotherapy. (IAEA-TECDOC-506) IAEA, Vienna, pp 193–199
22. Grosswendt B, Waibel E (1978) Transport of low energy electrons in nitrogen and air. Nucl Instr Methods 155: 145–156
23. Goulet T, Jay-Gerin J-P (1989) Thermalization of subexcitation electrons in solid water. Radiat Res 118: 46–62
24. Hatano Y, Inokuti H (1995) Photoabsorption, photoionization and photodissociation cross sections. In: Atomic and molecular data for radiotherapy and radiation research, Chapter 5. (IAEA-TECDOC-799) IAEA, Vienna
25. Pimblott SM, Mozumder A (1991) Structure of electron tracks in water. 2. Distribution of primary ionization and excitations in water radiolysis. J Phys Chem 95: 7291–7300
26. Bednar J (1985) Electronic excitations in condensed biological matter. Int J Radiat Biol 48: 147–166
27. LaVerne JA, Mozumder A (1993) Concerning plasmon excitation in liquid water. Radiat Res 133: 282–288
28. Turner JE, Magee JL, Wright HA, Chatterjee A, Hamm RN, Ritchie RH (1983) Physical and chemical development of electron tracks in liquid water. Radiat Res 96: 437–449
29. Hill MA, Smith FA (1994) Calculation of initial and primary yields in the radiolysis of water. Radiat Phys Chem 43: 265–280
30. Turner JE, Hamm RN, Wright HA, Ritchie RH, Magee JL, Chatterjee A, Bolch WE (1988) Studies to link the basic radiation physics and chemistry of liquid water. Radiat Phys Chem 32: 503–510
31. Ritchie RH, Hamm RN, Turner JE (1994) Interactions of low-energy electrons with condensed matter: relevance for track structure. In: Varma MN, Chatterjee A (eds) Computational approaches in molecular radiation biology. (Basic Life Sciences 63) Plenum Press, New York, pp 33–44
32. Green NJB, Pimblott SM (1989) Asymptotic analysis of diffusion-influenced kinetics with a potential. J Phys Chem 93: 5462–5467
33. Green NJB, Pilling MJ, Pimblott SM, Clifford P (1990) Stochastic modeling of fast kinetics in a radiation track. J Phys Chem 94: 251–258
34. Elliot AJ, McCracken DR, Buxton GV, Wood ND (1990) Estimation of rate constants for near-diffusion-controlled reactions in water at high temperatures. J Chem Soc Faraday Trans 86: 1539–1547
35. Buxton GV, Greenstock CL, Helman WP, Ross AB (1988) Critical review of rate constants for reactions of hydrated electrons, hydrogen atoms and hydroxyl radicals ($\cdot OH/\cdot O^-$) in aqueous solution. J Phys Chem Ref Data 17: 513–886
36. Pimblot SM, Green NJB (1992) Stochastic modeling of partially diffusion-controlled reactions in spur kinetics. J Phys Chem 96: 9338–9348
37. Pimblott SM, Pilling MJ, Green NJB (1991) Stochastic models of spur kinetics in water. Radiat Phys Chem 37: 377–388
38. Lide DR (ed) (1993) CRC handbook of chemistry and physics, 74th ed
39. Jonah CD, Matheson MS, Miller JR, Hart EJ (1976) Yield and decay of the hydrated electron from 100 ps to 3 ns. J Phys Chem 80: 1267–1270
40. Jonah CD, Miller JR (1977) Yield and decay of the OH radical from 200 ps to 3 ns. J Phys Chem 82: 1974–1976
41. Sumiyoshi T, Katayama M (1982) The yield of hydrated electrons at 30 picoseconds. Chem Lett: 1887–1890
42. Clifford P, Green NJB, Oldfield MJ, Pilling MJ, Pimblott SM (1986) Stochastic models of multi-species kinetics in radiation-induced spurs. J Chem Soc Faraday Trans 1, 82: 2673–2689
43. Watanabe R, Usami N, Kobayashi K (1995) Oxidation yield of the ferrous ion in a Fricke solution irradiated with monochromatic synchrotron soft X-rays in the 1.8 – 10 keV region. Int J Radiat Biol 68: 113–120
44. Konovalov VV, Raitsimring AM, Tsvetkov YuD (1988) Thermalization lengths of "subexcitation electrons" in water determined by photoinjection from metals into electrolyte solutions. Radiat Phys Chem 32: 623–632

45. Zaider M, Vracko MG, Fung AYC, Fry JL (1994) Electron transport in condensed water. Radiat Prot Dosim 52: 139–146
46. Pimblott SM (1992) Investigation of various factors influencing the effect of scavengers on the radiation chemistry following the high-energy electron radiolysis of water. J Phys Chem 96: 4485–4491
47. Pimblott SM, LaVerne JA (1994) Models for the radiation chemistry of aqueous solutions. Radiat Prot Dosim 52: 183–188
48. Roots R, Okada S (1975) Estimation of life times and diffusion distances of radicals involved in X-ray-induced DNA strand breaks or killing of mammalian cells. Radiat Res 64: 306–320
49. Tomita H, Kai M, Kusama T, Aoki Y (1995) Strand break formation in plasmid DNA irradiated in aqueous solution: effect of medium temperature and hydroxyl radical scavenger concentration. J Radiat Res 36: 46–55
50. Paretzke HG, Turner JE, Hamm RN, Ritchie RH, Wright HA (1991) Spatial distributions of inelastic events produced by electrons in gaseous and liquid water. Radiat Res 127: 121–129
51. Kutcher GJ, Green AES (1976) A model for energy deposition in liquid water. Radiat Res 67: 408–425
52. Ashley JC (1982) Stopping power of liquid water for low-energy electrons. Radiat Res 89: 25–31
53. Turner JE, Hamm RN (1995) Effects of elastic and inelastic scattering in giving electrons tortuous paths in matter. Health Phys 69: 378–384